RSC Advances

ROYAL SOCIETY OF CHEMISTRY

www.rsc.org/advances

Cite this: DOI: 10.1039/c0xx00000x

www.rsc.org/xxxxxx

ARTICLE TYPE

Soft-templated $LiFePO_4$/mesoporous carbon nanosheets (LFP/meso-CNSs) nanocomposite as the cathode material of lithium ion batteries

Ruofei Wu, Guofeng Xia, Shuiyun Shen, Fengjuan Zhu, Fengjing Jiang and Junliang Zhang*

Received (in XXX, XXX) Xth XXXXXXXXX 20XX, Accepted Xth XXXXXXXXX 20XX

DOI: 10.1039/b000000x

A novel and facile in-situ soft-templated method is proposed for synthesizing LFP/mesoporous carbon nanosheets (LFP/meso-CNSs) nanocomposite, which involves solvent evaporation induced self-assembly of triblock copolymers, with resol and inorganic as co-precursor of CNSs and LFP, followed by heat treatment. The LFP/meso-CNSs nanocomposite displays an excellent high-rate capability (122.1mA h/g at 5 C and 102.1 mA h/g at 10 C) and stable cycling property as the cathode material of lithium ion batteries, benefitting from its high electronic conductivity, open mesoporosity, and the nano-size of its active material.

Introduction

The growing environmental issues combined with fast depletion of fossil fuels, make the searching for energy storage and conversion devices with high efficiency and low emissions more and more imperative. Because of their relatively high operational voltage, high energy density and long cycle life, rechargeable lithium ion batteries (LIBs) are considered to be one of the most promising candidates, however, there still exist some challenges before their future practical applications in electric vehicles (EVs) and large-scale energy storage.[1-3] Among the various types of cathode materials, olivine lithium iron phosphate ($LiFePO_4$, LFP) has attracted more and more attention owing to its many significant advantages, including the high theoretical capacity (170 $mAhg^{-1}$), long cyclability, low toxicity, low cost and high safety.

Although appealing and promising, there remain a number of challenging problems in LFP to be resolved before its widespread commercialization. Both the low intrinsic electrical conductivity (10^{-9} ~ 10^{-10} S/cm) and low lithium-ion diffusivity (10^{-14} S/cm) greatly restrict the power performance of LFP[1-4]. In the past decade, intensive efforts have been devoted to improve the electrical conductivity and lithium-ion diffusivity of LFP by minimizing its particle size,[5-7] coating LFP with electronically conductive materials,[8-10] customizing particle morphologies,[11-13] and aliovalent-cation substitution[14-19]. More specifically, the electronic conductivity of LFP can be generally improved by being coated with conductive materials or doped with supervalent cations.[20] However, it is hard to achieve uniform surface coating and intra-doping in crystal.[21-23] In addition, although the lithium-ion diffusivity can be improved by tailoring the particle size to the nanoscale, the fabrication of nanoparticles is difficult under a high temperature process that is needed to obtain a high crystallinity. Moreover, the as-obtained nanoparticles possess high interfacial energy and are consequently prone to agglomerate, which severely offsets their merits.[24] Therefore, it is very important to design new and effective hierarchical architectures to avoid detrimental influences on the practical applications of LFP in LIBs.[25]

Recently, it was reported that mesoporous carbon-based composite materials with hierarchical structures, high specific surface area and high porosity could improve the electrochemical performance of electrode materials.[26-28] This was attributed to the fact that the active materials were well dispersed and no agglomeration formed, thus shortening the diffusion path length of lithium ions and maximizing the interfacial contact between the electrolyte and the active material. Moreover, the use of mesoporous carbon as the conductive and porous matrix could offer a three-dimensional (3D) conductive network for LIBs.[29]

So far, the study on mesoporous carbon-based composites as the anode material has been extensively carried out, including those containing Si,[30] Co_3O_4,[31] MnO_2,[32, 33] MoO_2,[34] SnO_2,[35] TiO_2,[36, 37] and $Li_4Ti_5O_{12}$.[38] Cao et al. synthesized $Li_4Ti_5O_{12}$/mesoporous carbon nanocomposite by the nanocasting technique using the porous carbon material CMK-3 as a hard template.[39] The conductive carbon network, ordered mesoporous structure and small nanocrystallites increase the ionic and electronic conduction throughout the electrode, and thus exhibited an improved electrochemical performance compared with bulk $Li_4Ti_5O_{12}$, i.e., 161.7 *vs.* 142.3 mAh/g at a rate of 0.2C. Zhou et al. reported a mesoporous carbon-silica-titania material using the tetra-constituents co-assembly method, and the composite material anode exhibited a high capacity of 875 mAh/g and a high initial efficiency of 56%.[40]

Unfortunately, the use of mesoporous carbon based composites as the cathode material of LIBs has rarely been reported, and this is owing to the fact that the heat treatment at a high temperature, a necessary step for the synthesis of cathode materials, could cause large grains of crystallites which may eventually destroy the nanoporous structure.[41-43] Xia et al. successfully prepared well-ordered mesoporous spinel-structured $LiMn_2O_4$ using the mesoporous silica KIT-6 as the template, and the cathode made of the as-obtained mesoporous $LiMn_2O_4$ maintained 94% of its initial capacity after 500 cycles and kept 80% of its reversible capacity at 0.1C rate, even at 5C rate.[44] $FePO_4$ loaded on large mesoporous carbon by Yang et al.

possessed excellent electrical conductivity, unique 3D porous structure, ultrahigh surface area, and other advantages.[45] Wang et al. prepared LFP/ mesoporous carbon nanocomposites by the nanocasting technique.[46] It was demonstrated that the nanocomposites exhibited a good specific capacity with an excellent cyclability. Jung et al. synthesized FeF_3/mesoporous carbon nanocomposites using mesoporous carbon as the template, and at current rates of 0.5C and above, the discharge capacities of the nanocomposites were 3 times larger than the corresponding values for bulk FeF_3.[47] It is noted that the above mentioned mesoporous carbon-based cathode materials are mainly based on a hard-templated route that is a complex process involving multiple steps such as impregnation of a silica template with a carbon precursor followed by carbonization of the resulting composite and the template removal, and thus it is not suitable for the large-scale synthesis.[47-49] In contrast, the soft-templated method is a viable and economically feasible strategy because it directly uses inexpensive and environmentally friendly surfactants as the structure-directing agents and no complex steps are needed [50].

Herein, we propose a novel and facile route for synthesizing LFP/mesoporous carbon nanosheets (LFP/meso-CNSs) nanocomposite via an in-situ soft-templated method, which involves solvent evaporation induced self-assembly (EISA) of triblock copolymers with resol and inorganic as co-precursor of CNSs and LFP followed by heat treatment. The mesoporous carbon matrix of the LFP/meso-CNSs filled with electrolyte not only serves as the mixed conducting network for both lithium ions and electrons to migrate to LFP nanoparticles but also restrains the nanocrystal growth during the heat treatment process and prevents them from aggregating during cycling, and thus the use of LFP/meso-CNSs nanocomposite as the cathode material of LIBs confers both excellent rate capability and cycle stability.

Experimental Section

Materials

All chemicals used were of analytical grade, and no further purification was performed. Phenol, formalin solution (37 wt%), sodium hydroxide, hydrochloric acid, ethanol, concentrated aqueous H_3PO_4 solution (85 wt%) and ethanol were purchased from Shanghai Chemical Industrial Co. Ltd. (Shanghai, China). $FeCl_2{\cdot}4H_2O$ (99%), LiCl(99.5%), and F127 (Pluronic block copolymer EO_{106}-PO_{70}-EO_{106}) were obtained from BASF Corp. All solutions were prepared in deionized (DI) water.

Synthesis of LFP/meso-CNSs nanocomposite

Soluble resol precursors were prepared by using phenol and formaldehyde in a base-catalyzed process according to the procedure reported previously.[51] The LFP/meso-CNSs nanocomposite was synthesized through a soft-templated method. In a typical procedure, $FeCl_2{\cdot}4H_2O$, H_3PO_4 and LiCl were used as the starting materials in a molar ratio of 1: 1: 1.01, and absolute ethanol was applied as the solvent. First, 2 g F127 was dissolved in 15 mL absolute ethanol under magnetic stirring to form a clear solution. Then, 5.0 g of the resol precursor solution (20 wt % in ethanol) was added dropwise and stirred for 10 min. Subsequently, $FeCl_2{\cdot}4H_2O$ and LiCl were transferred into the above solution. The mixture was vigorously stirred under flowing nitrogen to avoid the oxidation of Fe^{2+} until all the salts were dissolved, and H_3PO_4 was slowly added to the solution. After further stirring for 12 h, the mixture was cast onto Petri dishes, followed by the evaporation of ethanol for 8 h at room temperature in a hood. The resulted sticky films were subjected to thermocuring at 100 °C under vacuum for 24 h. The as-obtained composite films were ground into powders, and pyrolyzed in a tube furnace to decompose the triblock copolymer template and carbonize the phenolic resin, thus LFP nanocrystallites were in-situ generated. Specifically, the LFP/meso-CNSs nanocomposite were obtained by pyrolyzing the composite powders at 400 °C for 5 h followed by milling, then at 650 °C for another 8 h under the atmosphere of Ar containing 5% H_2 with a heating rate of 1 °C min^{-1}. For an electrochemical performance comparison, the bare LFP was prepared by the same process without the addition of F127, resol precursor solution or both of them.

Characterization

The X-ray powder diffraction (XRD) patterns of LFP/meso-CNSs composite were obtained using the Rigaku D\max-2200 instrument operating at 40 kV and 40 mA using CuKα radiation (λ = 0.154 nm), and the scanning ranged from 10° to 90°. The morphologies and compositions were characterized by transmission electron microscopy (TEM, JEOL 200CX), scanning electron microscopy (SEM, JEOL JSM-6700F), electron energy disperse spectroscopy (EDS, OXFORD INCA) and atomic force microscopy (AFM, IMODE NANOSCOPE, DI, USA). Raman spectra were recorded in a Renishaw inVia Raman microscope using the 514 nm lasers as a light source. Thermogravimetric analysis (TGA-209F3, NETZSCH, Germany) were performed at a heating rate of 5 °C /min under a flow of air. N_2 adsorption-desorption isotherms were measured on a QUADRASORB SI surface area & pore size analyzer at 77 K after the as-prepared samples were annealed at 200 °C.

Electrochemical testing

The working electrode was fabricated by mixing the as-synthesized active materials (80 wt%), carbon black (10 wt%) and polyvinylidene fluoride (PVDF 10 wt%), with N-methyl-2-pyrrolidone (NMP) used as the solvent. The slurry was evenly spread onto Al foil and dried at 120 °C for 24 h under vacuum. The electrochemical performance was tested by assembling CR2025 coin cells, using Li metal as the counter and reference electrode. The electrolyte solution was 1 M $LiPF_6$ in a 1:1 mixture of ethylene carbonate (EC) and dimethyl carbonate (DMC). The galvanostatic charge /discharge measurement was performed within a potential range of 2.0-4.2 V (vs. Li^+/Li) on a battery test system (LAND CT2001A, Wuhan Jinnuo Electronics, Ltd., China). Cyclic voltammetry (CV) and electrochemical impedance spectroscopy (EIS) tests of the cells were carried out at the scan rate of 0.1, 0.2, 0.4, 0.6, and1.0 mVs^{-1}, respectively, using an electrochemical workstation (CHI660C, Shanghai Chenhua, China). All the electrochemical measurements were conducted at room temperature.

Results and discussion

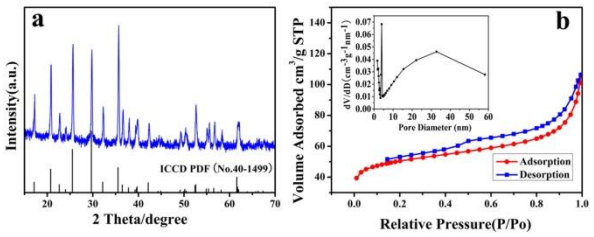

Fig.1 (a) X-ray diffraction pattern, (b)Nitrogen adsorption/desorption isotherms of the LFP/meso-CNSs nanocomposite, the inset is the pore-size distribution plot calculated by the BJH formula in the desorption branch isotherm.

Fig.1a shows the XRD pattern of the as-synthesized LFP/meso-CNSs nanocomposite. It is seen that all the diffraction peaks agree well with the orthorhombic LFP phase, indicating that LFP is well formed using this method. N_2 adsorption-desorption measurements were conducted to investigate the porous nature and the BET surface areas. As can be observed in Fig.1b, the LFP/meso-CNSs nanocomposite exhibits a hysteresis hoop at the high relative pressure, and it can be identified as type IV isotherms and characteristic of mesoporous structure.[52] The specific surface area of the LFP/meso-CNSs nanocomposite is $80.5 m^2 g^{-1}$, and it has a pore size distribution with a maximum of about 4 nm and 33 nm, which can be attributed to the removal of the organic moieties during pyrolysis and interspaces between LFP and mesoporous carbon nanosheets, respectively.[53] The representative thermogravimetric analysis (TGA) curve under air atmosphere in Fig.S1 indicates an appreciable weight loss between 350 and 600 °C, which is mainly ascribed to the carbon loss in the composite. As reported, the oxidation of $LiFePO_4$ to $Li_3Fe_2(PO4)_3$ and Fe_2O_3 can result in a weight gain of 5.07%.[54-56] After calculation from the TGA curves (see ESI, Fig. S1), the mesoporous carbon content is 9.27 wt% (5.07 + 4.20 %).

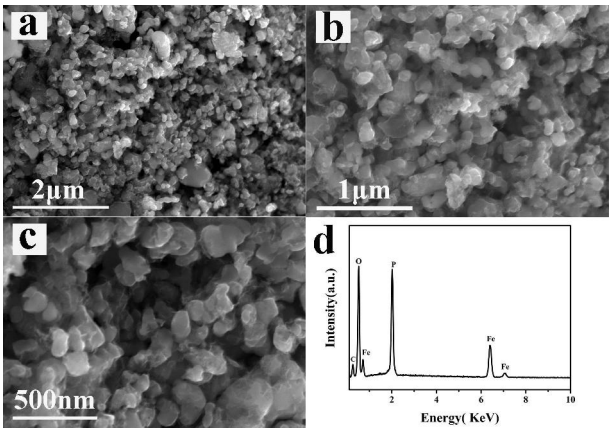

Fig.2 (a-c) Typical SEM images of the LFP/meso-CNSs nanocomposite, (d) Corresponding EDS spectrum.

Fig.2 shows SEM images of the LFP/meso-CNSs nanocomposite with different magnifications. As shown in Fig. 2a, the LFP nanoparticles are well dispersed in millimeter-sized monolithic pieces. According to the closer observation in Fig.2b-c, the LFP particles are monodispersed in the carbon nanosheets with a size ranging from 100 to 200 nm. Furthermore, the presence of voids and interspaces between the LFP particles and mesoporous carbon nanosheets obviously increases the surface area of the cathode material and promotes the intimate contact between the electrolyte and active materials. The existence of meso-CNSs can not only contributes to the improvement of the electronic conductivity of the inter-granular, but also restrains the nanocrystal growth during the heat treatment process and prevents them from aggregation while cycling extends. As can be seen in Fig.2d, the compositions are further confirmed by the elemental signatures of Fe, P, O and C.

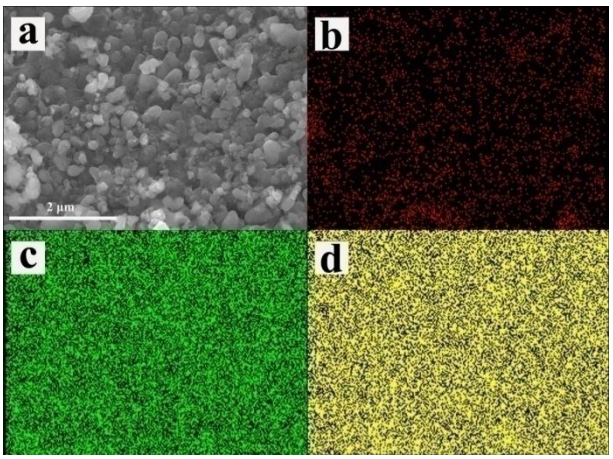

Fig.3 (a) Typical SEM images of LFP/meso-CNSs nanocomposite, (b-d) The corresponding elemental mappings of C, Fe and P elements in the composite by SEM-EDS.

A typical SEM image of the LFP/meso-CNSs nanocomposite and its corresponding elemental mappings are shown in Fig. 3. It is clearly observed that CNSs is uniformly distributed in the nanocomposite, demonstrating a well-interconnected conducting network. Meanwhile, Fe and P elements are well dispersed in the nanocomposite.

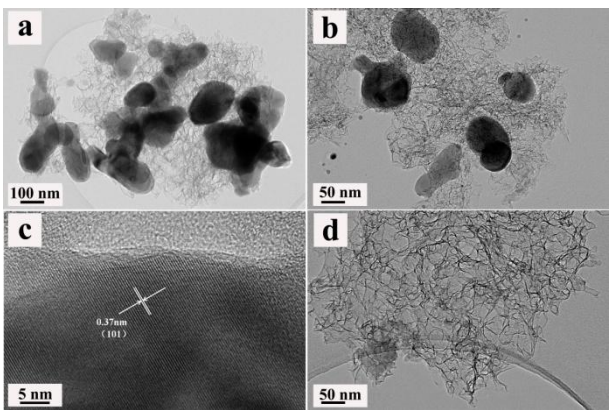

Fig.4 Typical TEM (a-b) and HRTEM (c) images of the LFP/meso-CNSs nanocomposite and typical TEM image (d) of the remaining CNSs obtained after removing LFP from the LFP/meso-CNSs nanocomposite using concentrated HCl solution.

The fine structure of the LFP/meso-CNSs nanocomposite was

further examined by TEM and the result is shown in Fig.4. It is observed that LFP particles are homogeneously anchored or embedded in the meso-CNSs. It is worth noting that the phenolic resol precursors provide active sites for LFP nuclei,[31] and thus promote the in-situ crystallite growth of anchored LFP nanoparticles. It is seen from Figs.4a and 4b that there also exist disordered mesopores in the CNSs, resulting from by the removal of F127 template and burn-out of C, H and O from the phenolic resin framework during pyrolysis. The wormhole mesopores are expected to provide a short diffusion path during lithium-ion insertion and extraction.[57] Fig. 4c shows the HRTEM image of LFP. The plane spacing is 0.37 nm corresponding to the (101) plane of orthorhombic LFP crystals and confirms a highly crystalline nature of the LFP, and this is consistent with the XRD result.

To further explore the structure of LFP/meso-CNSs nanocomposite, the composite were immersed in a concentrated HCl solution, and then LFP was removed and meso-CNSs were left. The representative TEM image of the remaining CNSs are shown in Fig.4d, the crumpled and thin nanosheets are obviously observed. In addition, it is also observed that some pores with a size ranging from 100nm to 200nm are distributed in the carbon nanosheets, indicating that some LFP nanoparticles were embedded in the carbon nanosheets. A typical AFM image (Fig.S2) reveals that the meso-CNSs have a dimenssion of several micrometers and the height difference between carbon nanosheets is ~ 5 nm (the green and red correspond to 1.169 nm and 4.304 nm, respectively).The Raman spectrum of the remaining CNSs in Fig.S3 shows two prominent peaks associated with sp^2 carbon(G-band,1597 cm^{-1}) and sp^3carbon (D-band, 1351 cm^{-1}), and this can be attributed to the in-plane vibrations of disordered amorphous carbon (D band) and crystalline graphic carbon (G band), respectively. The intensity ratio of G to D bands (I_G/I_D) is an indicator of the degree of graphitization. The I_G/I_D value of the CNSs is larger than those of previously reported the mesoporous carbon,[46,51,58] clearly showing that our CNSs is partially composed of graphitic structures.

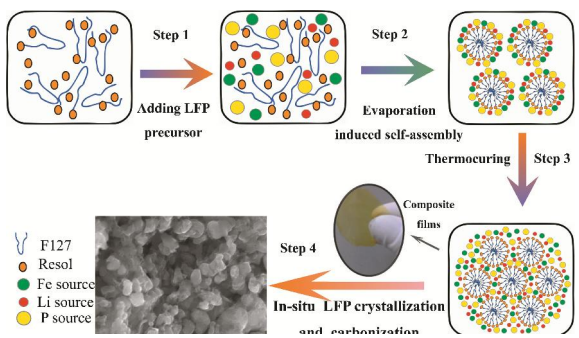

Scheme 1 Schematic illustration of synthesis of the LFP/meso-CNSs nanocomposite.

Based on the above experimental results, it is proposed that the LFP/meso-CNSs nanocomposite be synthesized through an in-situ soft-templated method, which involves solvent evaporation induced self-assembly (EISA) of triblock copolymer F127 with resol and inorganic as co-precursors of CNSs and LFP followed by heat treatment. The proposed fabrication procedure of LFP/meso-CNSs nanocomposite is schematically illustrated in Scheme 1. Triblock copolymer F127 and resol precursor are first dissolved in ethanol to form a homogeneous solution，and then the inorganic precursors of LFP are added. It is noted that the resol precursor has lots of phenolic hydroxyl groups, which not only interact with the hydrophobic EO chains of F127 via hydrogen bonding but also coordinate with the inorganic precursor of LFP.[31] Along with continuous evaporation of ethanol at room temperature, the interactions between the amphiphilic F127 macromolecules with resol and inorganic precursor of LFP become stronger, and the assembly of the co-precursors of CNSs and LFP proceed more easily. In the subsequent thermocuring process, the cross-linked structure of the co-precursors of LFP and CNSs is formed. Finally, the as-obtained composite films is pyrolyzed to decompose the triblock copolymer template at 400 °C and carbonize the phenolic resin at 650 °C, and thus LFP nanocrystallites are likely in-situ generated as their reaction temperature of 650 °C being the same as that of the carbonization of the phenolic resin phase. It should also be noted that when the weight ratio of LFP/mesoporous carbon is increased to (90wt%/10wt%), the LFP/meso-CNSs nanocomposite can be successfully synthesized by using the synergistic effect between the co-precursors of CNSs and LFP during the synthesis process.[36] The LFP nanocrystallites can thus be homogeneously separated by the meso-CNSs. In addition, when comparing the SEM and TEM results from the LFP/mesoporous carbon with a different ratio (70wt%/30wt%) in Fig.S4, it is demonstrated that the wall thickness of mesoporous carbon decreases with the increase in the weight ratio of LFP/mesoporous carbon.

By combining high electronic conductivity, open mesoporosity, and nanosized active material, it is expected that the LFP/meso-CNSs nanocomposite owns potential applications in high rate capability and good cycling stability as the cathode material of lithium ion batteries.

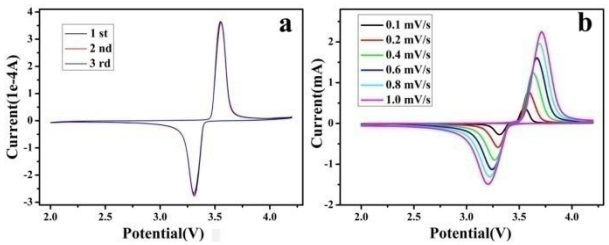

Fig.5 (a) the initial 3 CV curves at 0.1mVs^{-1}, (b) CV curves of the LFP/meso-CNSs composite electrode at different scanning rates.

The electrochemical performance of LFP/meso-CNSs nanocomposite was evaluated by CV and galvanostatic charge/discharge cycling using CR2025 coin cells. Fig.5a shows the CV curves at a scan rate of 0.1 mV s^{-1} within the potential window of 2.0-4.2 V (vs. Li/Li^+). The curves of the first three cycles at the scan rate of 0.1 mVs^{-1} are showed in Fig.5a. A pair of well-defined redox current peaks are observed between 3.2 and 3.7 V in the curves, and this is ascribed to the redox reaction of Fe^{2+}/Fe^{3+}.[59, 60] Fig.5b shows the CV curves at different potential scan rates ranging from 0.1 to 1 mV s^{-1}. The CV curve obtained at 0.2 mV s^{-1} shows an oxidation peak at 3.58 V and a reduction peak at 3.29 V. These peaks can also be clearly observed at a scan

rate of 1 mV s^{-1}, an oxidation peak at 3.69 V and a reduction peak at 3.21 V. It can therefore be concluded that the small redox-peak-potential difference at different scanning rates reveals an excellent reversibility of the synthesized material during insertion and extraction reaction of lithium ions.

Fig.6a shows the charge/discharge curves of the LFP/meso-CNSs composite electrode at different current rates. At the rate of 0.1 C (1 C = 170 mA/g), the discharge capacity of the composite electrode is 165.8 mAh/g, which is very close to the theoretical capacity of LFP. The discharge capacities at the current rates of 0.2 C, 0.5 C, 1 C, 2 C, and 5 C are 152.8, 147.3, 145.0, 135.3 and 122.1 mAh/g, respectively. Although the specific capacity gradually decreases with the increase in the current rate, it still possesses a capacity of 122.1 mAh/g at 5 C.

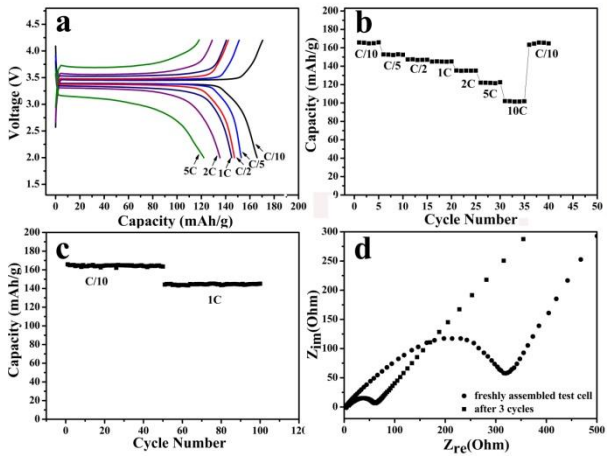

Fig.6 Electrochemical properties of the LFP/meso-CNSs composite electrode, (a) The typical charge and discharge curves at different current rates, (b) Rate performances,(c) cyclic performance when cycled at 0.1C and 1C rates, (d) EIS profiles of the LFP/meso-CNSs composite electrode in freshly assembled test cell after 3 cycles.

During the rate capacity tests, the charge-discharge cycles started with a low current rate of 0.1C for the initial 5 cycles, and then the rates gradually increased up to 10C. As shown in Fig.6b, even at the high current rate of 10 C, a capacity of 102.1mAh/g is still obtained. It is noted that when the current rate is reversed back to 0.1 C, the reversible capacity of the composite electrode returns to 165 mAh/g, indicating an excellent capacity reversibility. It is worth noting the rate performance of the composite electrode is comparable or even better than those of previously reported LFP composites synthesized using glucose,[52,61] citric acid,[62,63], dopamine[64] as a carbon source or even directly using hard templated porous carbon as conductivity additive.[65,66] These results indicated that our LFP/meso-CNSs nanocomposite offered a high initial discharge capacity at 0.1 C and excellent rate capability, which were attributed to the structural features of the nanocomposite and will be discussed in detail in the following section.

It is well known that the cycling stability of the electrode at a high discharge rate is very important for practical applications. As shown in Fig.6c, after the composite electrode being cycled at a rate of 0.1C for over 50 cycles, no significant capacity loss is detected. Even at a rate of 1C and after 50 cycles, the capacity retention remains as high as about 98%, indicating a remarkable cyclic performance.

Fig. 6d shows the Nyquist plots that consist of a depressed semicircle in the high frequency region followed by an oblique line in the low frequency region. The former is due to the charge-transfer reaction at the electrode/electrolyte interfaces, and the latter represents the Warburg impedance, which is associated with lithium ions diffusion in the bulk of the electrode.[67,68] As shown in Fig 6d, a high charge-transfer resistance (R_{ct}) is a feature of the freshly assembled cell. After three charge/discharge cycles, the R_{ct} is reduced to about 60 Ω. It is reasonable to assume that the reduction of resistance is due to the structures of the composite electrode allowing fast penetration of electrolyte and maximizing the interfacial contact between electrolyte and active material.

In order to confirm the role of the unique structural features of the nanocomposite in more detail, the bare LFP was prepared by the same process without the addition of F127, resol precursor solution or both of them. For an electrochemical performance comparison, the rate capabilities of bare LFP at various charge-discharge rates were showed in Fig.S5. The bare LFP only maintained discharge capacities of 119.4 mAh/g at 0.1C, 96.5 mAh/g at 1C, 76.8 mAh/g at 5C, and 57.8mAh/g at 10C respectively, all of which were much lower than those of our LFP nanocomposite. As shown in Fig.S6, the Rct of bare LFP is about 300 Ω after three charge/discharge cycles, which is much higher than our LFP nanocomposite.

Because of the low intrinsic electrical conductivity of LFP, the electrons in the bare LFP electrode will reach the relatively limited positions where lithium ion intercalation takes place, thus resulting in limited the reaction area. In addition, lithium ion diffusion to LFP active sites is kinetically hindered in the bare LFP electrodes, thus the degree of polarization of the electrode increases with each charge-discharge cycle and finally leads to poor rate capability. As shown in Fig.S7, the significantly improved electrochemical performance of LFP/meso-CNSs nanocomposite can be attributed to its high electronic conductivity, open mesoporosity, and the nano-size of its active material, which can enhance the electronic and ionic conductivity throughout the electrode.

Based on the above mentioned experimental results, the LFP/meso-CNSs nanocomposite exhibited an excellent electrochemical performance, and this is mainly ascribed to the unique composite architecture resulting from the following factors. First, nano-sized and high-crystallinity LFP nanoparticles are in-situ generated in the monolithic carbon matrix, which shortens the diffusion-path length of lithium ions and maximizes the interfacial contact between electrolyte and active material. Second, the meso-CNSs can offer efficient transport pathways for lithium ion diffusion to LFP active sites, which have been demonstrated to be beneficial for the high-rate electrochemical performance.[31,39,49] Finally, plenty of voids and interspaces in monolithic composite architecture can further increase the surface area of the composite and promote an intimate contact between the electrolyte and active materials.

Conclusions

In conclusion, the LFP/meso-CNSs nanocomposite was

successfully synthesized by means of a facile in-situ soft-templated method, which involved a solvent–evaporation-induced self-assembly (EISA) of triblock copolymers with resorcinol and inorganic as the co-precursors of LFP and meso-CNSs followed by heat treatment. It is demonstrated that the LFP/meso-CNSs electrode has an excellent electrochemical performance especially with a high-rate capability and stable cycling properties, as a result of its high electronic conductivity, open mesoporosity, and the nano-size of its active material. Both the unique structure and promising performance of the LFP/meso-CNSs nanocomposite indicate that the as-proposed facile approach provides a potentially general pathway for the development of high-performance electrodes with low-conductivity active materials for applications in electric vehicles and energy storage.

Acknowledgements

We gratefully acknowledge the financial support from the Natural Science Foundation of China under contract No. 21373135, PSA Peugeot Citroën, and Shanghai Municipal Education Commission for the award of Eastern Scholar Professorship.

Notes and references

Address, Institute of Fuel Cells, MOE Key Laboratory of Power & Machinery Engineering, Shanghai JiaoTong University, Dongchuan Road 800, 200240, Shanghai, China. Fax: +86-21-3420-7439; Tel: +86-21-3420-6239; E-mail:junliang.zhang@sjtu.edu.cn

† Electronic Supplementary Information (ESI) available: [Fig. S1–S4]. See DOI: 10.1039/b000000x/

1 M. Takahashi, S.-i. Tobishima, K. Takei and Y. Sakurai, *Solid State Ionics*, 2002, **148**, 283-289.
2 A. Andersson and J. O. Thomas, *J. Power Sources*, 2001, **97**, 498-502.
3 C. Benoit and S. Franger, *J. Solid State Electrochem.*, 2008, **12**, 987-993.
4 X. Rui, X. Zhao, Z. Lu, H. Tan, D. Sim, H. H. Hng, R. Yazami, T. M. Lim and Q. Yan, *ACS nano*, 2013,**7**,5637-5646.
5 Y.-q. Wang, J.-l. Wang, J. Yang and Y. Nuli, *Adv. Funct. Mater.*, 2006, **16**, 2135-2140.
6 R. Malik, D. Burch, M. Bazant and G. Ceder, *Nano Lett.*, 2010, **10**, 4123-4127.
7 C. Delacourt, P. Poizot, S. Levasseur and C. Masquelier, *Electrochem. Solid-State Lett.*, 2006, **9**, A352-A355.
8 H. Huang, S.-C. Yin and L. S. Nazar, *Electrochem. Solid-State Lett.*, 2001, **4**, A170-A172.
9 N. Ravet, Y. Chouinard, J. Magnan, S. Besner, M. Gauthier and M. Armand, *J. Power Sources*, 2001, **97**, 503-507.
10 K. S. Park, S. B. Schougaard and J. B. Goodenough, *Adv. Mater.*, 2007, **19**, 848-851.
11 S. Yang, P. Y. Zavalij and M. Stanley Whittingham, *Electrochem. Commun.*, 2001, **3**, 505-508.
12 Y. Wang, Y. Wang, E. Hosono, K. Wang and H. Zhou, *Angew. Chem. Int. Ed.*, 2008, **47**, 7461-7465.
13 L. Wang, X. He, W. Sun, J. Wang, Y. Li and S. Fan, *Nano Lett.*, 2012, **12**, 5632-5636.
14 S.-Y. Chung, J. T. Bloking and Y.-M. Chiang, *Nat .Mater.*, 2002, **1**, 123-128.
15 C. Sun, Z. Zhou, Z. Xu, D. Wang, J. Wei, X. Bian and J. Yan, *J. Power Sources*, 2009, **193**, 841-845.
16 H. C. Shin, S. B. Park, H. Jang, K. Y. Chung, W. I. Cho, C. S. Kim and B. W. Cho, *Electrochim. Acta*, 2008, **53**, 7946-7951
17 K.-F. Hsu, S.-Y. Tsay and B.-J. Hwang, *J. Power Sources*, 2005, **146**, 529-533.
18 H. Xie and Z. Zhou, *Electrochim. Acta*, 2006, **51**, 2063-2067.
19 M.-R. Yang and W.-H. Ke, *J. Electrochem. Soc.*, 2008, **155**, A729-A732.
20 X.-m. Liu, P. Yan, Y.-Y. Xie, H. Yang, X. Shen and Z.-F. Ma, *Chem. Commun.*, 2013.**49**, 5396-5398.
21 M. S. Islam, D. J. Driscoll, C. A. Fisher and P. R. Slater, *Chem. Mater.*, 2005, **17**, 5085-5092.
22 M. Wagemaker, B. L. Ellis, D. Lützenkirchen-Hecht, F. M. Mulder and L. F. Nazar, *Chem. Mater.*, 2008, **20**, 6313-6315.
23 C. A. Fisher, V. M. Hart Prieto and M. S. Islam, *Chem. Mater.*, 2008, **20**, 5907-5915.
24 P. G. Bruce, B. Scrosati and J. M. Tarascon, *Angew. Chem. Int. Ed.*, 2008, **47**, 2930-2946.
25 J.-M. Tarascon and M. Armand, *Nature*, 2001, **414**, 359-367.
26 X. W. D. Lou, L. A. Archer and Z. Yang, *Adv. Mater.*, 2008, **20**, 3987-4019.
27 Q.F. Zhang, E. Uchaker, S. L. Candelaria and G. Z.Cao, *Chem. Soc. Rev.*,2013. **42**, 3127-3171.
28 J. Ming, J.-B. Park and Y.-K. Sun, *ACS Appl. Mat. Interfaces*, 2013, **5**, 2133-2136.
29 J.L. Adcock, P. F. Fulvio,and S. Dai, *J. Mater. Chem. A*, 2013.1.9327-9331.
30 Z. Wang, F. Li, N. S. Ergang and A. Stein, *Carbon*, 2008, **46**, 1702-1710.
31 Z.K. Sun, B. Sun, M.H. Qiao, J. Wei, Q. Yue, C. Wang, Y.H. Deng, S. Kaliaguine and D. Y.Zhao, *J. Am. Chem. Soc.*, 2012, **134**, 17653-17660.
32 X.P. Dong, W.H. Shen, J.L. Gu, L.M. Xiong, Y.F. Zhu, H. Li and J.L. Shi, *J. Phys. Chem.* B, 2006, **110**, 6015-6019.
33 S. Zhu, H. Zhou, M. Hibino, I. Honma and M. Ichihara, *Adv. Funct. Mater.*, 2005, **15**, 381-386.
34 Y.F. Shi, B.K. Guo, S. A. Corr, Q. H.Shi, Y.-S. Hu, K. R. Heier, L. Chen, R. Seshadri and G. D. Stucky, *Nano Lett.*, 2009, **9**, 4215-4220.
35 H. Kim and J. Cho, *J. Mater. Chem.*, 2008, **18**, 771-775.
36 P.-y. Chang, C.-h. Huang and R.-a. Doong, *Carbon*, 2012, **50**, 4259-4268.
37 Y. G. Guo, Y. S. Hu, W. Sigle and J. Maier, *Adv. Mater.*, 2007, **19**, 2087-2091.
38 L.F.Shen, E. Uchaker, C.Z. Yuan, P. Nie, M. Zhang, X.G. Zhang and G.Z. Cao, *ACS Appl. Mat. Interfaces*, 2012, **4**, 2985-2992.
39 L.F.Shen, X. G.Zhang, E. Uchaker, C.Z. Yuan and G.Z. Cao, *Adv. Energy Mater.*, 2012, **2**, 691-698.
40 Y.Y.Zhou, Y.H.Kim, C.S.Jo, J.W.Lee, C.W.Lee, and S.H.Yoon. *Chem. Commun.*, 2011, **47**, 4944-4946.
41 R. Dominko, M. Bele, J.-M. Goupil, M. Gaberscek, D. Hanzel, I. Arcon and J. Jamnik, *Chem. Mater.*, 2007, **19**, 2960-2969.
42 P.D. Yang, D.Y. Zhao, D. I. Margolese, B. F. Chmelka and G. D. Stucky, *Nature*, 1998, **396**, 152-155.
43 S. L.Wang, Z.X. Zhang, S.H. Fang, L. Yang, C.C. Yang and S.-i. Hirano, *Electrochim. Acta*, 2013.**111**,685-690.
44 J.Y. Luo, Y.G. Wang, H.M. Xiong and Y.Y. Xia, *Chem. Mater.*, 2007, **19**, 4791-4795.
45 L. Chen, P. Wu, K.W. Xie, J.P. Li, B. Xu, G.P. Cao, Y. Chen, Y.W. Tang, Y.M. Zhou, T.H. Lu and Y.S. Yang, *Electrochim. Acta*, 2013, **92**, 433-437.
46 G.X. Wang, H. Liu, J. Liu, S.Z. Qiao, G. M. Lu, P. Munroe and H. Ahn, *Adv. Mater.*, 2010, **22**, 4944-4948.
47 H. Jung, J. Shin, C. Chae, J. K. Lee and J. Kim, *J. Phys. Chem.C*, 2013, **117**, 14939-14946.
48 S. Lim, C. S. Yoon and J. Cho, *Chem. Mater.*, 2008, **20**, 4560-4564.
49 C. M. Doherty, R. A. Caruso, B. M. Smarsly, P. Adelhelm and C. J. Drummond, *Chem. Mater.*, 2009, **21**, 5300-5306.
50 S. Tanaka, Y. Katayama, M. P. Tate, H. W. Hillhouse and Y. Miyake, *J. Mater. Chem.*, 2007, **17**, 3639-3645.
51 Y. Meng, D. Gu, F.Q. Zhang, Y.F. Shi, H.F. Yang, Z. Li, C.Z. Yu, B. Tu and D.Y. Zhao, *Angew. Chem. Int. Ed.*, 2005, **117**, 7215-7221.
52 J.Q. Zhao, J.P. He, J.H. Zhou, Y.X. Guo, T. Wang, S.C Wu, X.C. Ding, R.M. Huang and H. R.Xue, *J. Phys. Chem.C*, 2011, **115**, 2888-2894.
53 C.M. Doherty, R. A. Caruso and C. J. Drummond, *Energy Environ. Sci.*, 2010, **3**, 813-823.
54 X.M. Lou and Y.X. Zhang, *J. Mater. Chem.*, 2011, **21**, 4156-4160.

55 S.F.Yang,P.Y.Zavalij and M.S.Whittingham, *Electrochem.Commun*., 2001, **3**, 505- 508.

56 J.L. Yang, J.J.Wang, Y.J.Tang, D.N.Wang, X.F.Li, Y.H. Hu, R.Y. Li, G.X. Liang, T.-K. Sham and X.L. Sun, *Energy Environ. Sci*., 2013, **6**, 1521-1528.

57 Y. Fang, Y.Y. Lv, R.C. Che, H.Y. Wu, X.H. Zhang, D. Gu, G.F. Zheng and D.Y. Zhao, *J. Am. Chem. Soc*., 2013, **135**, 1524-1530.

58 J. Tang, Y.Y. Wu, E. W. McFarland and G. D. Stucky, *Chem. Commun.*, 2004, 1670-1671.

59 J.L. Yang, J.J. Wang, Y.J. Tang, D.N. Wang, B.W. Xiao, X.F. Li, R.Y. Li, G.X. Liang, T.-K. Sham and X. L. Sun, *J. Mater. Chem. A*, 2013. **1**, 7306-7311.

60 C.Y.Wu, G.S. Cao, H.M. Yu, J. Xie and X.B.Zhao, *J. Phys. Chem.C*, 2011,**115**, 23090-23095.

61 Z. R. Chang, H. J. Lv, H. W. Tang, H. J. Li, X. Z. Yuan and H. Wang, *Electrochim. Acta*, 2009, **54**, 4595-4599.

62 F. Yu, J.J. Zhang, Y.F. Yang and G.Z. Song, *J. Power Sources*, 2009, 189,794-797.

63 C. Sun, S. Rajasekhara, J. B. Goodenough and F. Zhou, *J. Am. Chem. Soc*., 2011, **133**, 2132-2135.

64 Z.X. Chi, W. Zhang, F.Q. Cheng, J. T. Chen, A.M. Cao and L.J. Wan, *RSC Adv*., 2014, **4**,7795-7798

65 H.F. Ni, J.K. Liu and L.Z. Fan, *Nanoscale*, 2013, **5**, 2164-2168.

66 C. M. Doherty, R. A. Caruso, B. M. Smarsly and C. J. Drummond, *Chem. Mater*., 2009, **21**, 2895-2903.

67 A. Vu and A. Stein, *Chem. Mater.*, 2011, **23**, 3237-3245.

68 B. Wang, D.L. Wang, Q.M. Wang, T.F. Liu, C.F. Guo and X.S. Zhao, *J. Mater. Chem. A*, 2013, **1**, 135-144.

Abstract: soft-templated LFP/mesoporous carbon nanosheets (LFP/meso-CNSs) nanocomposite as the cathode of lithium ion batteries, displays an excellent high-rate capability and stable cycling property, benefitting from its high electronic conductivity, open mesoporosity, and the nano-size of its active material.